

# QUANTIFICATION OF MICROCRACK CHARACTERISTICS AND IMPLICATIONS FOR STIFFNESS AND STRENGTH OF GRANITE

Luke Griffiths<sup>1</sup>, Michael J. Heap<sup>1</sup>, Patrick Baud<sup>1</sup>, and Jean Schmittbuhl<sup>1</sup>

\* Corresponding author: L. Griffiths ([luke.griffiths@unistra.fr](mailto:luke.griffiths@unistra.fr))

## ABSTRACT

Microcracks can affect the mechanical properties of rocks, such as their stiffness and strength. To provide a link between the microstructural parameters and the mechanical behaviour of rock, micromechanical models use parameters that represent a quantitative description of the microcrack population. However, these parameters are difficult to constrain. With the aim of better constraining micromechanical models for rock strength and stiffness, we provide here robust measurements of microcrack characteristics. We developed an algorithm to process optical micrographs of rock, automatically creating binary images of the microcrack network. We applied this procedure to optical micrographs of fine-grained granite samples that have undergone varying degrees of thermal microcrack damage. From these processed images, we calculate the mean microcrack length and the number of microcracks per unit area (and therefore the 2D microcrack density). We also create heat maps showing the spatial distribution of microcracks and their lengths. The results of our automated image analysis are in very good agreement with those of widely-used stereological techniques, and we show that our method can be applied to other rock types (sandstone and andesite) that contain microcracks. Using the measured microcrack characteristics as inputs for the Ashby and Sammis (1990) 2D micromechanical sliding wing crack model, we predict the uniaxial compressive strength of the granite and compare the predictions with strength measurements made in the laboratory. We find good agreement between the model and the experimental data for granite heated to temperatures below the alpha-beta transition of quartz (~573 °C). Rock strength is overestimated above this threshold, possibly due to variations in fracture toughness, which is considered constant in our modelling. Finally, we use the 2D sliding crack model of David et al. (2012) to infer microcrack density and aspect ratio from the mechanical response of the thermally microcracked samples to cyclic stressing. We show a good agreement between inferred and measured crack densities if a scaling factor is introduced.

**Keywords:** segmentation; image analysis; microcrack; crack density; micromechanical model; scaling.

## 1 INTRODUCTION

Rocks commonly contain microscopic cracks (Kranz, 1983; Simmons and Richter, 1976). Microcracks in rock have a length of typically 0.1 mm or less (Simmons and Richter, 1976) and an aspect ratio, i.e. the ratio of their aperture and their length, of less than  $10^{-2}$ , generally in the range of  $10^{-3}$ – $10^{-5}$ . They can be mechanically, chemically, or thermally induced and significantly affect the thermal (Kant et al., 2017) and transport (Le Ravalec et al., 1996; Nasser et al., 2009; Siratovich et al., 2015) properties of rock, which may have important implications for geothermal or hydrocarbon reservoirs, or for the underground storage of nuclear waste (Paterson and Wong, 2005). Microcracks also reduce the stiffness (Budiansky and O'Connell, 1976; Jaeger et al., 2009; Simmons et al., 1975; Walsh, 1965; Zimmerman, 1985) and strength (Jaeger et al., 2009; Paterson and Wong, 2005) of rocks, an important consideration for

industrial geomechanical problems such as borehole break-outs (Bérard and Cornet, 2003) and natural geophysical phenomena, including the formation and properties of fault zones (Mitchell and Faulkner, 2009).

As a result, the detailed microscale characterisation of rock must inform on the mechanical response at the laboratory scale and beyond, and numerous micromechanical models exist to perform such a function. For example, one type of up-scaling model relies on the scale invariance of fracture processes (Bonnet et al., 2001). Another type assumes a clear representative elementary volume at the micro-scale and up-scales to greater lengthscales using micromechanical damage mechanics models. Examples of the latter include micromechanical models that explore the influence of microcracks on rock stiffness (Budiansky and O'Connell, 1976; David et al., 2012; Walsh, 1965) and strength (Ashby and Sammis, 1990; Griffith, 1921; McClintock and Walsh, 1962; Murrell and

<sup>1</sup>Institut de Physique de Globe de Strasbourg, Université de Strasbourg/EOST, CNRS UMR 7516, France.

Digby, 1970). The reliability of these micromechanical models depends on the accuracy of the micro-scale characterisation, along with the adequacy of the model assumptions for a given rock. For instance, micromechanical models for failure require an accurate description of the initial microcrack density and geometry. In the case of Ashby and Sammis' 2D sliding wing crack model (Ashby and Sammis, 1990), which predicts the compressive failure of microcracked materials and has been widely applied to the failure of rocks (Baud et al., 2014; Baud et al., 2000; Rawling et al., 2002), an initial crack damage parameter is required, itself a function of the microcrack length and the number of microcracks per unit area (herein referred to as the number density). However, these micromechanical models typically show some limitations when the crack density becomes large and multiple crack interactions are in play up to the limit of the microcrack coalescence (Hansen and Schmittbuhl, 2003; Ortiz, 1988; Wong et al., 2001). A central issue of modelling damage mechanics is the consideration of microcrack interactions for high microcrack densities (e.g. Hashin (1988), Horii and Nemat-Nasser (1986), and Kemeny and Cook (1991)).

To obtain information on the microcrack distribution, microscopy is one of the most commonly used tools. For example, a quantification of the microcrack density may be obtained "manually" using the stereological techniques of Underwood (1967) (see Fredrich et al. (1989), Heap et al. (2009b, 2014a), Tapponnier and Brace (1976), Wong (1985), and Wu et al. (2000)). These established techniques involve placing a grid over a microscope image and counting intersections between microcracks and the grid to calculate their area density. However, this manual approach can be time consuming and is open to subjectivity. Microcrack characteristics can also be determined numerically from digital images of the microcrack network (dedicated analysis tools are available, for example FracPac (Healy et al., 2017)). These images can be generated manually by tracing over micrographs (which has subjectivity and reproducibility issues) or automatically, using image segmentation techniques to create binary images of the microcracks. For example, Arena et al. (2014) and Delle Piane et al. (2015) used image processing software to segment backscattered Scanning Electron Microscopy (SEM) micrographs of Carrara Marble. From the processed SEM micrographs, they are able to calculate the microcrack length, aspect ratio and surface density. For studying microcracks, SEM micrographs have the advantage over optical micrographs in that they are sensitive to mass density. However, compared to optical microscopy, SEM is more expensive, time consuming, and technically demanding. For analyses of large sets of micrographs, it is therefore of interest to develop an automated and robust procedure targeting optical micrographs.

In this study, we aim to address the influence of microcrack density on the mechanical response of rock. To keep other rock attributes such as the mineralogy and grain size con-

stant, we selected a fine-grained granite (Garibaldi Grey Granite) in which we induced varying amounts of thermal microcracking by heating samples to temperatures ranging from 100 to 900 °C. To assess the thermal microcrack damage on the microscale, we present here a new automatic procedure, coded in Python, that rapidly extracts quantitative microcrack statistics from optical microscope images. The details of the micrograph processing stage, which produces binary images of the microcracks, are described in Supplementary Materials. From the processed images, we calculate the microcrack length and number density, thus quantifying the microcrack damage present within the rock (scripts for both the image processing and the microcrack quantification are available on demand from the corresponding author). We then performed uniaxial deformation experiments to study the influence of thermal microcracking on rock stiffness and uniaxial compressive strength (UCS). We compare our experimental UCS measurements on the thermally microcracked granite samples with the upscaled predictions from Ashby and Sammis' micromechanical sliding wing crack model (Ashby and Sammis, 1990) (using data from our quantitative microcrack analysis). Finally, we followed a downscaling approach by using the sliding crack model of David et al. (2012) to infer values of the microcrack density and aspect ratio using data from stress-cycling experiments on the thermally microcracked granite, and we compare these values to the direct microscale measurements.

## 2 MATERIALS AND METHODS

Previous studies that focus on the influence of microcrack density on the physical and mechanical properties of rock have performed experiments on variably thermally microcracked samples of the same rock (e.g. David et al. (1999) and Wang et al. (2013)). In this way, the microcrack density may vary, whilst other rock properties such as composition and grain size remain constant. Here we follow the same approach by preparing a suite of variably thermally microcracked granite samples for our measurements.

### 2.1 Sample preparation

Garibaldi Grey Granite from British Columbia, Canada, was chosen for this study due its homogeneity and small crystal size (between 0.5 and 1 mm) with regards to the dimensions of a thin section and a laboratory sample. The composition of the granite, estimated from an optical micrograph of the unheated granite (a cropped micrograph is shown in Figure 1) is 45 % quartz, 45 % feldspar, and 10 % mica. For the laboratory measurements, we prepared 11 cylindrical samples of 20 mm diameter and nominally 40 mm in length and thermally

microcracked them to varying degrees by heating them in a furnace at room pressure to temperatures of 100, 200, 400, 500, 550, 600, 650, 750, 800, and 900 °C. One sample was left intact. The heating procedure consisted of drying the rock in a vacuum pump at 40 °C over 24 h before placing the sample in the furnace, programmed to heat at 1 °C/min to the desired maximum temperature. The rock remained at the target temperature for a dwell time of two hours before being cooled at 1 °C/min back to room temperature. Considering the low heating and cooling rate of 1 °C/min, we assume that the temperature gradient across our samples to be negligible. Indeed, the time constant for thermal equilibrium of a cylindrical sample is equal to  $r^2/d$  where  $r$  is sample radius and  $D$  is the thermal diffusivity (Wang et al., 2013). If we take the diffusivity of our 20 mm diameter granite samples to be that of Westerly Granite ( $1 \times 10^{-6} \text{ m}^2/\text{s}$ ) (Clauser and Huenges, 1995; Vosteen and Schellschmidt, 2003; Wang et al., 2013), the time constant is equal to 100 s. The time constant is within an order of magnitude of the 60 s the furnace takes to heat by 1 °C and, as such, we can expect a low thermal gradient across the sample. Figure 1 shows cropped optical micrographs of the intact granite (Figure 1a) and the granite heated to 600 °C (Figure 1b). The granite heated to 600 °C clearly contains more microcracks than the intact sample (Figure 1b).

## 2.2 Crack density and crack length measurements

Thin sections of the granite samples were prepared in a plane parallel to the sample axis. Optical microscope images at 2500× optical zoom ( $2592 \times 1944$  pixels, or  $5.2 \times 3.9$  mm) were taken across the entirety of each of the thin sections (that have an area of roughly  $20 \times 25$  mm, i.e. 100 % of the sample width and 62 % of the sample length). Figure 1 shows examples of cropped micrographs of the intact sample and the sample heated to 600 °C. All the cropped micrographs were processed to create binary images of the microcracks, following the filtering and segmentation procedure described in detail in Supplementary Materials. Microcracks were automatically identified and characterized in the processed images in windows of  $1 \times 1$  mm and their lengths were approximated by the distance between their end points.

Examples of entire thin section of the granite heated to 550, 600, and 650 °C are shown in Figure 2. Figure 2 also shows the spatial distributions (heat maps) of the number of cracks per unit area (or number density),  $N_A$ , and the mean microcrack length, calculated from the processed optical micrographs in windows of  $1 \times 1$  mm. We see no spatial preference for the location of microcracking, which supports our conclusion that the heating/cooling rate is sufficiently low to ensure a homogeneous temperature distribution within the sample. If this was not the case, we might expect a higher number of microcracks per unit area at the periphery of the sample. In these

examples, we generally observe an increase in  $N_A$  and a decrease in the mean microcrack length with temperature (Figure 2).

The final results of the image analysis are shown in Figure 3: the mean number of cracks per unit area, or number density  $N_A$ , and the mean microcrack length as a function of thermal stressing temperature (data also available in Table 1). Error bars represent one standard deviation from the mean microcrack length and number density. We see that  $N_A$  remains constant ( $\sim 75/\text{mm}^2$ ) up to a temperature of 550 °C.  $N_A$  is doubled from 550 to 600 °C (from  $\sim 75$  to  $\sim 150/\text{mm}^2$ ), but remains approximately constant (between  $\sim 150$  and  $\sim 175/\text{mm}^2$ ) between 650 and 900 °C (Figure 3). The calculated values of the microcrack lengths (100 μm or less) are compatible with values of microcrack lengths in the literature (see Kranz (1983) and Simmons and Richter (1976) and references therein). The mean microcrack length increases slightly with temperature up to around 550 °C (Figure 3). Above 550 °C, the mean microcrack length decreases to  $\sim 60$  μm and remains constant up to the maximum temperature of 900 °C (Figure 3).

To validate the proposed automatic procedure, we compared our analysis to the widely-used manual stereological techniques of Underwood (1967). The latter technique extracts information on the 3D microstructure from 2D microscope images to provide the surface area per unit volume,  $S_V$  ( $\text{mm}^{-1}$ ). For this, parallel test lines are drawn across the 2D image and the number of intersections between these lines and the features are counted. The number of intersections per unit length of test line is written  $P_L$  ( $\text{mm}^{-1}$ ). Assuming that the surfaces of the feature are randomly distributed within the volume and that a large number of parallel test lines are drawn, we have Equation 1 (Saltykov, 1958).

$$S_V = 2P_L \quad (1)$$

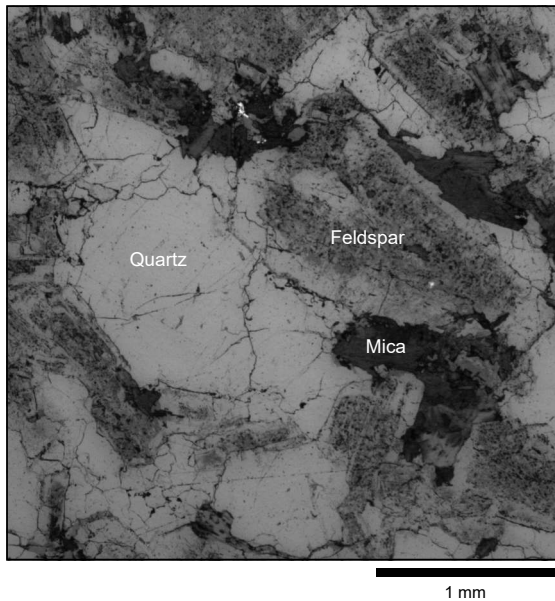
If we now consider two sets of test lines drawn in perpendicular directions, we have two values,  $P_I$ , the number of intersections per test line length in the first direction, and  $P_{II}$ , the number of intersections per test line length in the second direction.  $S_V$  is then equal to the sum of the intersections per unit length in both directions (Equation 2).

$$S_V = P_I + P_{II} \quad (2)$$

In our case, the features we consider are microcracks, and Figure 4a shows a grid of test lines overlaying a  $2 \times 2$  mm micrograph of the granite sample heated to 600 °C. Here the grid test lines are spaced at regular intervals of 0.1 mm, as used in Heap et al. (2009a) and Heap et al. (2014b). This example micrograph has also been processed following our algorithm (Figure 4b) and the resulting microcrack network is shown in



(a) Garibaldi Grey Granite, non-heated



(b) Garibaldi Grey Granite, heated to 600 °C

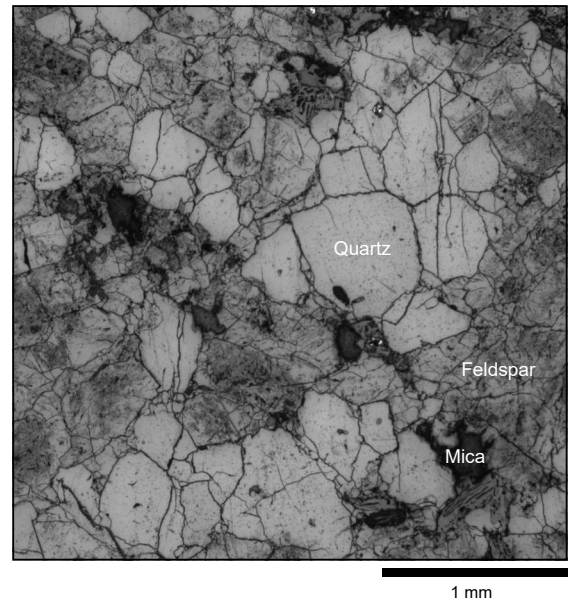


Figure 1: Cropped 3 mm × 3 mm optical micrographs of Garibaldi Grey Granite: (a) a thin section of the unheated granite and (b) a thin section of the granite which has been heated to 600 °C.

green. In this way, we can compare the  $S_V$  values from manually counting intersections between test lines and the microcracks in the original (i.e. unprocessed) microscope image with  $S_V$  values resulting from the automatic counting of intersections with the microcracks in the processed image. The result of this analysis is presented in Figure 5a. We see that  $S_V$  values obtained from manually counting intersections in the original image are very similar to those obtained by counting intersections programmatically in the processed image (Figure 5a). We note that the manual method is open to subjectivity and that results may vary from user to user.

For our analysis method, rather than use a grid, we chose to directly calculate  $N_A$  by automatically locating and counting cracks within 1 × 1 mm windows of the processed micrographs. To compare the two methods,  $S_V$  can be related to  $N_A$  through the Walsh (1965) 2D crack density,  $\gamma$ , which is defined by Equation 3, where  $c$  is the crack half-length.

$$\gamma = N_A c^2 \quad (3)$$

Through direct measurements of the mean crack length,  $2c$ , and  $N_A$ , Hadley (1976) showed an agreement between the product of these two values and the microcrack length per unit area of Underwood (1967) (Equation 4).

$$L_A \approx 2c N_A \quad (4)$$

$L_A$  is related to  $S_V$  via Equation 5 (Underwood, 1967) and therefore  $S_V$  can be used to calculate the 2D crack density,  $\gamma$  (Equation 6).

$$L_A = \frac{\pi}{4} S_V \quad (5)$$

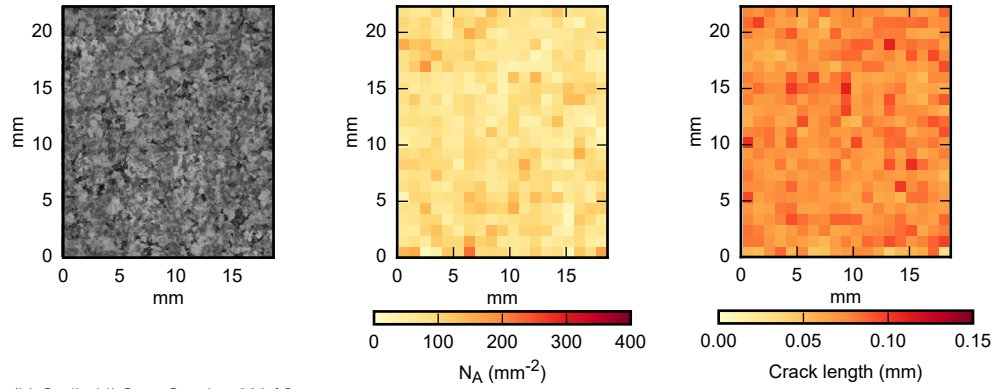
$$\gamma \approx \frac{\pi S_V c}{8} \quad (6)$$

For all thin sections,  $\gamma$  was calculated from both  $N_A$  and  $S_V$  (Figure 5b). Both methods give similar results, especially for lower values of  $\gamma$ . The strong agreement between the calculated values of  $N_A$  and  $S_V$  serves to validate the method (including the crack length approximation) and the accuracy of the stereological methods.

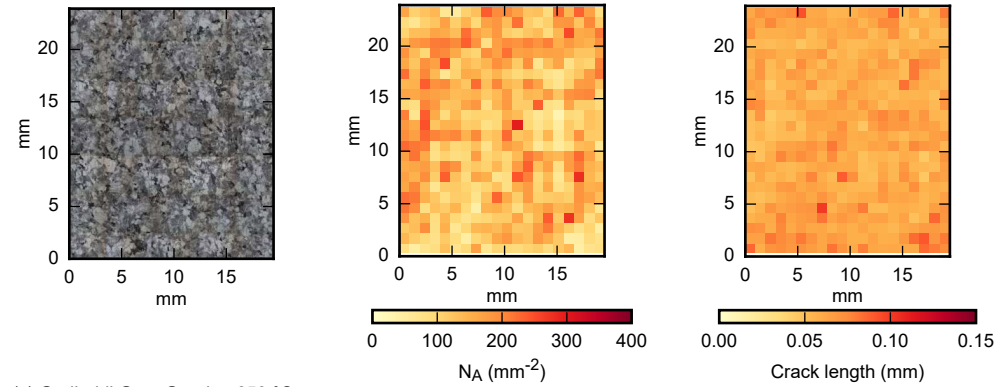
### 2.3 Physical properties (porosity and P-wave velocity)

The connected porosities of all granite samples were measured using the triple weight water saturation method. The P-wave velocities, noted  $v_P$ , were measured under ambient pressure and temperature conditions along the length of the oven-dried cylindrical samples (placed in a vacuum oven for at least 24 h at 40 °C). The porosity and  $v_P$  of the 11 samples were measured following the heating procedure and ranged, respectively, from 0.009 and 4.37 km/s for the intact rock to

(a) Garibaldi Grey Granite, 550 °C



(b) Garibaldi Grey Granite, 600 °C



(c) Garibaldi Grey Granite, 650 °C

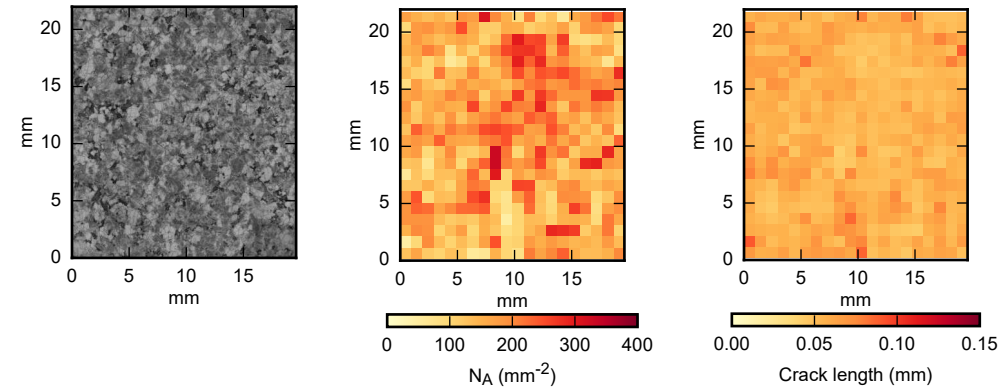


Figure 2: Original optical micrographs of thin sections of Garibaldi Grey Granite samples heated to (a) 550, (b) 600, and (c) 650 °C, alongside heat maps of the number of microcracks per unit area ( $N_A$ ) and the mean microcrack length ( $2c$ ) over a  $1 \times 1$  mm area, as calculated from the processed micrographs (data given in [Table 1](#)).

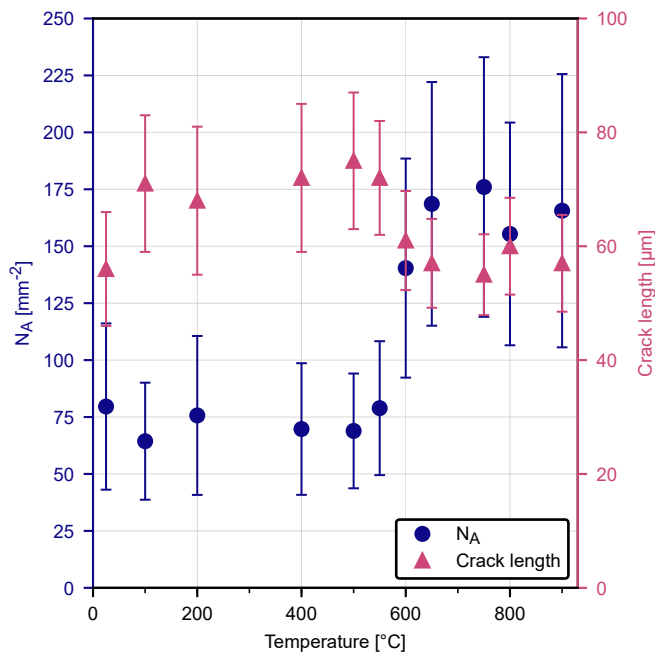


Figure 3: Results of the micrograph analysis of all Garibaldi Grey Granite thin sections. Shown are the mean number of microcracks per unit area ( $N_A$ ) and mean microcrack lengths ( $2c$ ) as a function of the maximum temperature to which the sample was heated. Error bars give one standard deviation from the mean number of cracks and their average lengths per mm<sup>2</sup> across each thin section.

Table 1: The results of the micrograph analysis of all Garibaldi Grey Granite thin sections. For each thermal stressing temperature, we report the calculated mean crack number density,  $N_A$ , and mean crack length,  $2c$ . From these values, we calculate the crack density,  $\gamma$  (Equation 3).

Thermal stressing temperature [°C]	Cracks per unit area $N_A$ [mm <sup>-2</sup> ]	Mean crack length $2c$ [μm]	2D crack density $\gamma$
ambient	79.6	56	0.062
100	64.4	71	0.081
200	75.7	68	0.088
400	69.7	72	0.090
500	68.9	75	0.097
550	78.9	72	0.102
600	140.4	61	0.131
650	168.6	57	0.137
750	176.0	55	0.133
800	155.4	60	0.140
900	165.6	57	0.135

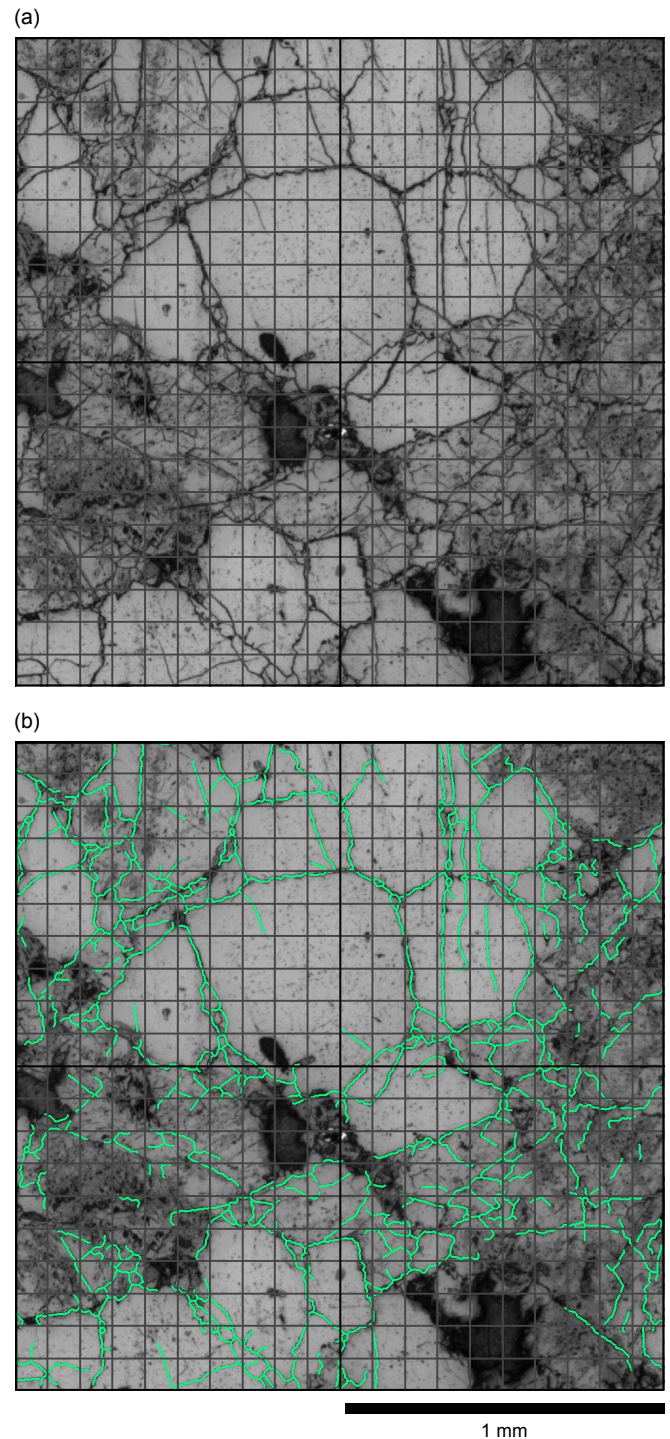


Figure 4: (a) Cropped micrograph of the thin section of Garibaldi Grey Granite sample heated to 600 °C. A grid has been superposed to show the working of the stereological method of Underwood (1967). (b) The same micrograph as in panel (a) with the results of micrograph processing (details provided in Supplementary Materials) superposed in green.

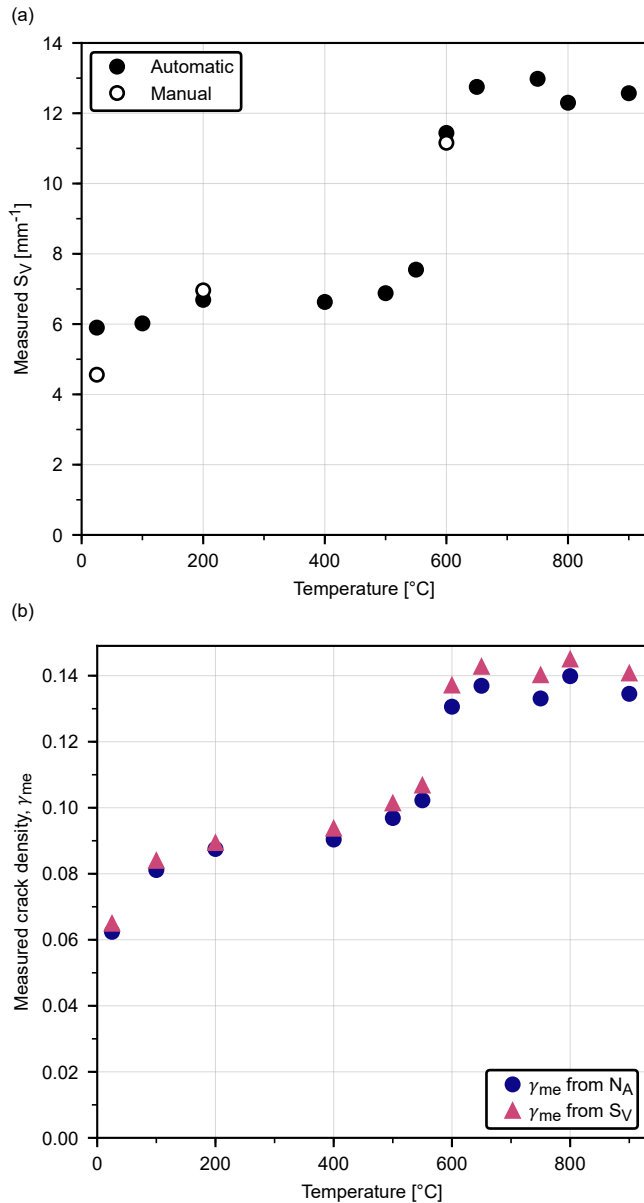


Figure 5: (a) Comparison between the mean crack surface area per unit volume ( $S_V$ ) from manually counting intersections between microcracks and test lines in the original 25, 200, and 600  $^{\circ}\text{C}$  micrographs (cropped to 10 x 10 mm) and  $S_V$  given by the number of intersections between the generated microcrack network and the test lines across the entire thin section. (b) The measured microcrack density ( $\gamma_{\text{me}}$ ) for each thin section of Garibaldi Grey Granite as calculated from both the microcrack number density  $N_A$  (Equation 3), and the crack surface per unit volume  $S_V$  (Equation 6).

Table 2: The physical properties of all Garibaldi Grey Granite samples measured at room temperature and pressure. For each maximum heating temperature, we report the connected porosity, the P-wave velocity,  $v_P$ , and the measured uniaxial compressive strength (UCS).

Thermal stressing temperature [ $^{\circ}\text{C}$ ]	Connected porosity	$v_P$ [km/s]	Measured UCS [MPa]
ambient	0.009	4.37	287
100	0.010	4.09	241
200	0.011	3.98	261
400	0.011	3.35	254
500	0.014	3.05	240
550	0.015	2.79	229
600	0.021	2.08	191
650	0.024	1.98	165
750	0.028	1.77	145
800	0.027	1.75	163
900	0.037	1.48	122

0.037 and 1.48 km/s for the sample heated to 900  $^{\circ}\text{C}$  (Table 2; Figure 6a). The porosity increases with the maximum heating temperature, whilst  $v_P$  decreases with temperature (Figure 6a). In both measurements, large changes are observed from 500 to 600  $^{\circ}\text{C}$  (Figure 6a). Since we observe no pores in the microstructural images (Figure 1) we assume that all porosity is cracks.

#### 2.4 Stiffness measurements

We conducted a series of deformation experiments in which we uniaxially loaded and unloaded each of the 11 oven-dry (under vacuum at 40  $^{\circ}\text{C}$  for at least 24 hours) samples (examples of these curves are shown in Figure 7a). Samples were loaded up to a maximum stress (within the elastic domain) at a constant strain rate of  $1 \times 10^{-5}$ /s. The maximum stresses for cycling were therefore chosen to be well below the UCS of the rock as not to induce cracking: 100 MPa for all samples heated up to 650  $^{\circ}\text{C}$  and less, and 75 MPa for the samples heated to 750, 800, and 900  $^{\circ}\text{C}$ . The axial strain was measured using a single strain gauge (Vishay Micro-Measurements 125UT general purpose strain gauge) glued halfway along the length of the sample, this way we eliminate any deformation of the load-train from the recorded data. A lubricating wax was applied to either end of the samples to limit any stress due to friction between the rock and the pistons (Bésuelle et al., 2000).



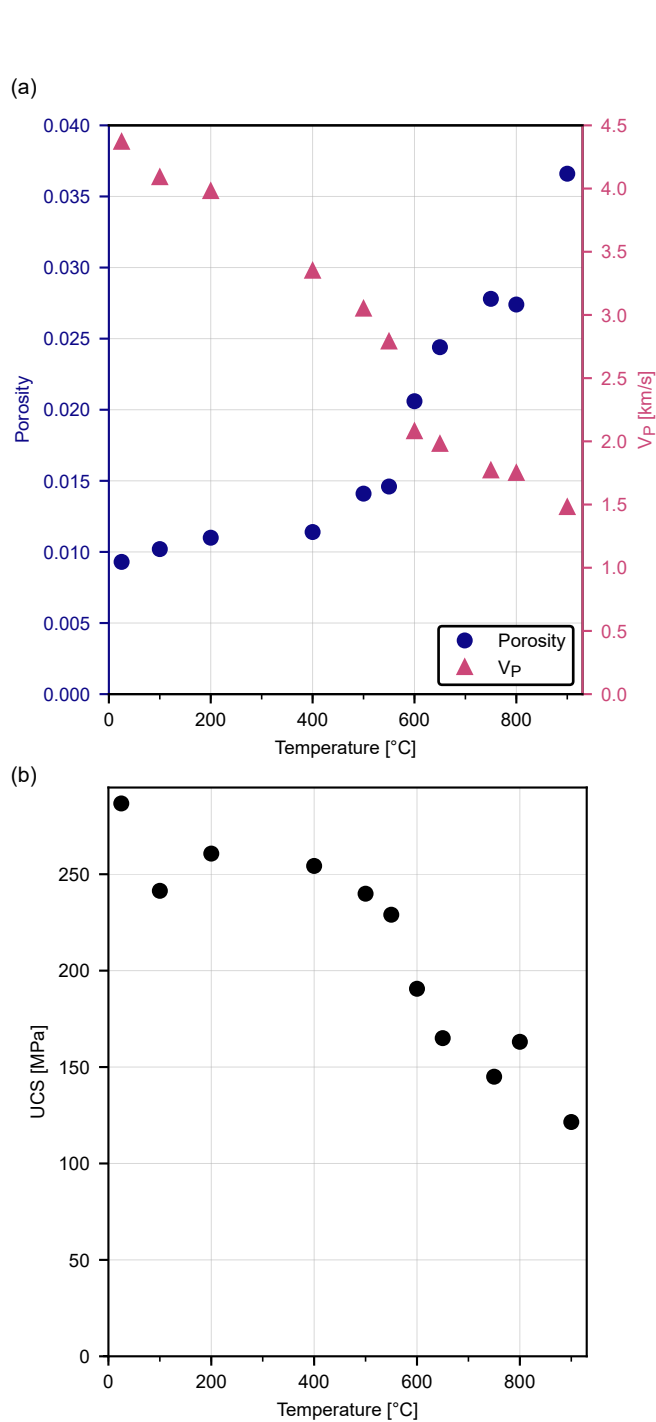


Figure 6: Physical and mechanical properties of the Garibaldi Grey Granite samples as a function of thermal stressing temperature: (a) the measured values of connected porosity and P-wave velocity, and (b) the uniaxial compressive strength (UCS).

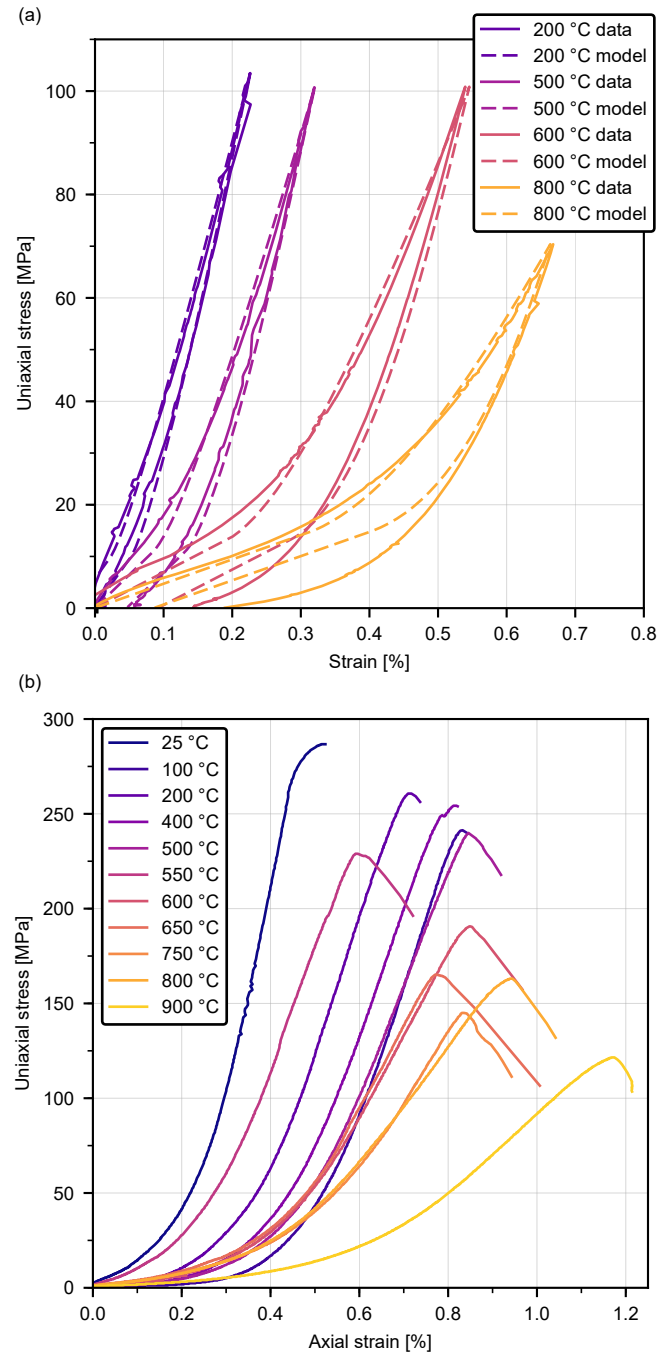


Figure 7: Mechanical testing of thermally stressed Garibaldi Grey Granite samples. (a) Axial stress against axial strain during uniaxial stress-cycling tests on samples heated to 200, 500, 600, and 800 °C. The 200, 500, and 600 °C samples were loaded to a maximum uniaxial stress of around 10 MPa, the 800 °C sample was loaded to a maximum stress of around 75 MPa. (b) Axial stress against axial strain for all uniaxial compressive strength (UCS) tests on the thermally stressed samples (25–900 °C).



### 2.5 Uniaxial compressive strength (UCS) measurements

UCS tests were conducted on the 11 oven-dry (under vacuum at 40 °C for at least 24 h) granite samples at a constant strain rate of  $1 \times 10^{-5}$ /s until failure, whilst measuring axial stress and strain (Figure 7b). Strain was calculated using data from a linear variable differential transducer (LVDT) that monitored the displacement of the piston relative to the static base plate. Displacement measured by the LVDT was corrected for the strain accumulated in the load-train. For all UCS tests, a lubricating wax was again applied to both ends of the sample to limit friction at the piston/sample interfaces. The measured values of UCS (Table 2) are shown in Figure 6b as a function of thermal stressing temperature. UCS generally decreases with temperature. For example, UCS was decreased from 287 MPa for the ambient sample to 122 MPa for the sample thermally stressed to 900 °C (Figure 6b). As for the porosity and  $v_P$  measurements (Figure 6a), we observe a notable change in UCS from 550 to 600 °C (Figure 6b).

## 3 MICROMECHANICAL MODELLING

### 3.1 Upscaling using the Ashby and Sammis 2D sliding wing crack model

Brittle failure is the result of the propagation, interaction, and coalescence of microcracks and as such, micromechanical models of rock failure, which are based on the work of Griffith (1921), must consider microcrack geometry. This is achieved by considering a certain microcrack density, often expressed as a single damage parameter, which evolves during brittle deformation. One of the most popular models is the 2D sliding wing crack model of Ashby and Sammis (1990). This model is based on linear elastic fracture mechanics applied to the failure of rocks in compression (Baud et al., 1996; Horii and Nemat-Nasser, 1986; Kemeny and Cook, 1991). It considers a planar far-field stress in which there is a microcrack of half-length  $c$  at a given angle to the maximum principal stress direction. As the far-field axial stress increases, the Coulomb condition for sliding is satisfied. The microcrack tips locally concentrate the tensile stress, which increases further with frictional slip along the microcrack. In this case, wing cracks may nucleate from each tip when the mode I (opening) stress intensity factor reaches a critical value, noted  $K_{IC}$ . The wing cracks then follow a curved path before aligning with the principal stress direction.

The sliding wing crack model (Ashby and Sammis, 1990) was developed for brittle failure of a material containing a certain density of microcracks, which propagate in the direction of the major principal stress if the material is loaded in compres-

sion. For geometrical simplicity, the model considers that all microcracks have the same half-length and the same orientation of 45 ° to the principal stress direction. Then, if the wing cracks become sufficiently proximal, microcrack interactions will lead to microcrack coalescence and, ultimately, macroscopic failure. For uniaxial compression, the sliding wing crack model (Ashby and Sammis, 1990) gives an expression for the applied stress  $\sigma_1$  as a function of  $\mu$ , the friction coefficient of the fracture,  $K_{IC}$ , the fracture toughness,  $c$ , the crack half-length,  $D$  the damage parameter, and  $D_0$  the initial damage parameter Equation 7b:

$$\sigma_1 = \frac{\frac{C_4}{\cos(45^\circ)} \frac{K_{IC}}{\sqrt{\pi c}} \sqrt{\sqrt{\frac{D}{D_0}} - 1 + \frac{0.1}{\cos(45^\circ)}}}{1 + \frac{\sqrt{\pi D_0}}{1 - \sqrt{D}} \left( \sqrt{\frac{D}{D_0}} - 1 \right)} \quad (7)$$

Where  $C_4 = \frac{\sqrt{30} \cos(45^\circ)}{\sqrt{1 + \mu^2 - \mu}}$ . The initial damage parameter  $D_0$  is proportional to the 2D microcrack density,  $\gamma$ , of Walsh (1965) by Equation 8b, which is in turn a function of the microcrack half-length,  $c$ , and the microcrack number density,  $N_A$  (Equation 3).

$$D_0 = \frac{\pi}{2} \gamma \quad (8)$$

The applied stress,  $\sigma_1$ , is therefore a function of the microcrack density, as the interaction between microcracks is important in the deformation process. The model predicts that for a certain level of damage  $D$  (increasing with the wing crack length), the applied stress,  $\sigma_1$ , will reach a peak: the UCS of the rock. An cedure is therefore necessary to determine the UCS using this model.

However, the initial damage in the rock,  $D_0$ , is often ill-constrained in studies that use the Ashby and Sammis model (Ashby and Sammis, 1990) as it requires knowledge of the microcrack distribution. Here we determine  $D_0$  from the rock microstructure by processing optical micrographs to calculate the mean microcrack length ( $2c$ ) and number density ( $N_A$ ). From the mean values of  $N_A$  and  $c$ ,  $D_0$  was calculated using Equation 3 and Equation 8 for each thin section (Table 3). We include all cracks, regardless of their orientation, in the calculation of  $D_0$ , and the sliding crack model assumes that they are all at 45 ° to the stress direction. We find that the unheated granite has a  $D_0$  of 0.098, which is comparable to that of Westerly Granite, a granite with similar porosity and crystal size, at 0.13 (Brace et al., 1966).  $D_0$  increases with temperature up to a temperature of 650 °C, after which  $D_0$  remains roughly constant up to the maximum temperature of 900 °C (Table 3).

The sliding wing crack model (Ashby and Sammis, 1990) (Equation 8) was then used to predict the UCS of the 11 samples

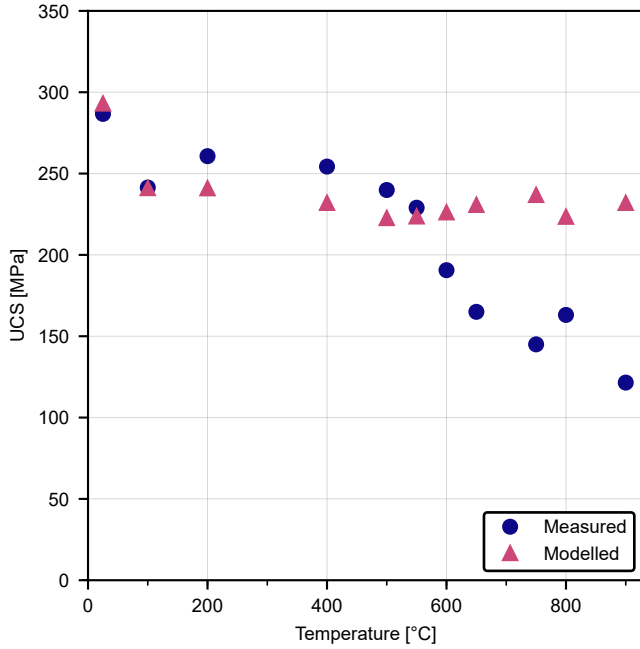


Figure 8: The laboratory-measured uniaxial compressive strength (UCS) and the UCS predicted by the sliding wing crack model (Ashby and Sammis, 1990) as a function of thermal stressing temperature for Garibaldi Grey Granite.

(Figure 8). The value of the fracture toughness  $K_{IC}$  and the friction coefficient,  $\mu$ , for the unheated granite were inferred by fitting the wing crack model to triaxial deformation experiments on unheated, oven-dry samples of Garibaldi Grey Granite at confining pressures of 0, 5, and 10 MPa. The calculated values of  $K_{IC}$  and  $\mu$  are  $0.54 \text{ MPa}\cdot\text{m}^{1/2}$  and 0.7, respectively, and were assumed constant for all samples. The values of  $D_0$  that result from our microstructural analysis are given in Table 3. We highlight that under some conditions, 2D modelling may require particular care when applied to 3D fracture processes (Germanovich et al., 1994), however, for predicting the stiffness, mechanical behaviour, and failure of 3D rock samples, 2D modelling has been used to great effect in a range of rock types (Baud et al., 2014; Griffiths et al., 2017; Heap et al., 2016).

### 3.2 Downscaling using the David et al. (2012) sliding crack model for the stiffness of damaged rock

The stiffness of rock is strongly influenced by microcracking (see Figure 7). During the uniaxial loading of microcracked rock, the stress-strain curves are characterized by a strong non-linearity and hysteresis (David et al., 2012; Walsh, 1965). With increasing uniaxial load, the first microcracks to close are those perpendicular to the direction of the applied

Table 3: The calculated values of the initial damage parameter  $D_0$ ,  $\frac{K_{IC}}{\sqrt{\pi c}}$ , and the predicted uniaxial compressive strength (UCS) provided by the sliding wing crack model (Ashby and Sammis, 1990) for temperatures between ambient and 900 °C.

Thermal stressing temperature [°C]	$D_0$	$\frac{K_{IC}}{\sqrt{\pi c}}$ [MPa]	Predicted UCS [MPa]
Ambient	0.098	58.0	293.0
100	0.127	51.5	241.0
200	0.137	52.6	240.9
400	0.142	51.2	231.9
500	0.152	50.1	222.6
550	0.161	51.2	223.6
600	0.205	55.6	226.1
650	0.215	57.5	230.7
750	0.209	58.5	236.8
800	0.220	56.0	223.4
900	0.211	57.5	231.9

stress, followed by those at lower angles. Once microcracks are closed they may begin to slide if the friction between the faces of the crack is overcome, meaning that the rock is always less stiff than it would be in the absence of microcracks (David et al., 2012; Walsh, 1965). The Walsh 2D sliding crack model (Walsh, 1965) provides the stiffness of a microcracked material during uniaxial compression as a function of the mean microcrack and microcrack density. The model was recently extended by David et al. (2012) to include the unloading of the material.

For a given uniaxial stress, a microcrack may be open, closed, or closed and sliding. If the microcrack is open or sliding, then it contributes to the stiffness of the rock. The contribution of the microcrack to the bulk Young's modulus depends on its aspect ratio, its orientation with regards to the applied stress direction, and the friction coefficient on the crack face. During loading, the effective Young's modulus is a function of the intact Young's modulus of the uncracked rock  $E_0$ , and the sum of the compliances of the open ( $C_{\text{open}}$ ) and sliding ( $C_{\text{sliding}}$ ) microcracks (Equation 9):

$$E_{\text{loading}} = \frac{E_0}{1 + C_{\text{open}} + C_{\text{sliding}}} \quad (9)$$

The Young's modulus during unloading is a function of the intact Young's modulus of the uncracked rock  $E_0$ , and the sum of the compliances of the open ( $C_{\text{open}}$ ) and reverse sliding ( $C_{\text{reverse}}$ ) microcracks (Equation 10):

$$E_{\text{unloading}} = \frac{E_0}{1 + C_{\text{open}} + C_{\text{reverse}}} \quad (10)$$

During loading, a microcrack may begin sliding once the ap-

plied stress reaches a certain value, depending on the crack orientation with regards to the stress and the friction coefficient. The stress-strain curve is initially steeper than previous because, for the microcracks to slide back towards their initial position, the Coulomb criteria along the crack face must be fulfilled in the opposite direction, thereby overcoming resistance to frictional sliding twice. Microcracks that were closed and sliding are now stuck and do not contribute to the effective Young's modulus. As a result, the slope of the curve at the very beginning of unloading is closer to the Young's modulus of the uncracked rock (Walsh, 1965). Microcracks begin sliding in the opposing direction only once the applied stress is sufficiently decreased and as such, this model predicts the hysteresis that we observe experimentally (Figure 7a).

To infer the microcrack density and aspect ratio of microcracks in the thermally stressed granite samples, we used the (David et al., 2012) to fit our uniaxial cyclic loading experimental curves (Figure 7a). The intact Young's modulus, equal to 65 GPa, was provided by the slope at the beginning of the unloading cycle. For comparison, the Voigt-Reuss-Hill average estimate (Hill, 1952) of the intact Young's modulus is 76 GPa if we assume: no porosity; a mineralogical composition in volume of 45 % quartz, 45 % feldspar and 10 % mica; and the elastic moduli of the minerals provided from Mavko et al. (2009). The Voigt-Reuss-Hill estimate is similar but greater than the measured value as it does not account for any microstructural elements which may contribute to rock stiffness (e.g. grain boundaries or pressure-independent microporosity), justifying our value of 65 GPa for the intact Young's modulus. The friction coefficient was set to 0.7, as for our UCS modelling. The microcrack aspect ratio and microcrack density were then selected manually to best fit the shape of the stress-strain curve. Figure 7a shows examples of the experimental curves (solid curves) and the best-fit curves (dashed curves) predicted by the model.

The inferred microcrack aspect ratios using the David et al. (2012) range from  $2.4 \times 10^{-4}$  to  $5 \times 10^{-4}$ , within the typical  $1 \times 10^{-3}$ – $1 \times 10^{-4}$  range for microcracks (Kranz, 1983) (Figure 9). The inferred microcrack densities range from 0.5 to 4.9 (noted  $\gamma_{mo}$  in Figure 9) and are similar to those inferred by David et al. (2012) from uniaxial cycling data of thermally stressed La Peyratte granite, which range from 0.2 for an intact sample to 4.4 for a sample heated to 600 °C. We see that both the inferred microcrack densities and aspect ratios increase with temperature, showing a marked increase between 550 and 650 °C (Figure 9).

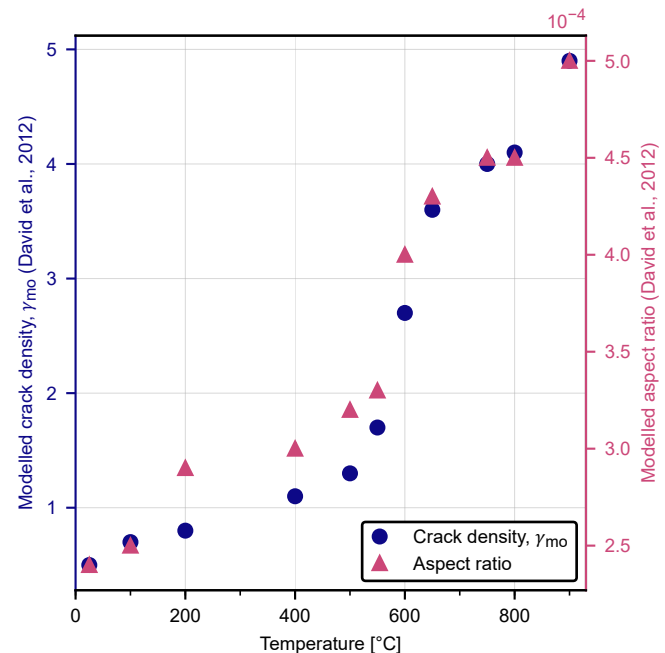


Figure 9: The mean microcrack density ( $\gamma_{mo}$ ) and aspect ratio in the thermally stressed Garibaldi Grey Granite, as inferred from the rock compressibility using the sliding crack model (David et al., 2012), against thermal stressing temperature. Some example experimental and modelled stress-strain curves are shown in Figure 7a.

## 4 DISCUSSION

### 4.1 Automated procedure for quantifying microcrack characteristics

We present here a new automated procedure (described in detail in Supplementary Materials) for rapidly processing optical micrographs of microcracked materials to quantify their microcrack characteristics. We calculate the mean microcrack length and number density to obtain the mean microcrack density (Equation 2). Further, we can create heat maps showing the spatial distribution of microcracks and their lengths (Figure 2). We found that for a suite of thermally microcracked granites, our automated procedure provides microcrack characteristics in very good agreement with those measured using widely-used stereological techniques (Underwood, 1967) (Figure 5). Our program therefore offers a reliable method to quickly and robustly determine microcrack characteristics of microcracked granites from optical micrographs. Although automated programs exist that can extract microcrack characteristics from images (e.g. Arena et al. (2014) and Delle Piane et al. (2015)) they, so far, have relied on SEM images, which are more time-consuming to collect and more expensive than

optical microscope images.

We have shown that our automated image analysis procedure works for optical micrographs of granite. To explore whether our algorithm works well for rock types with different microstructures, we analysed two additional thin sections: a deformed sample of Darley Dale Sandstone and an intact (but naturally microcracked) andesite from Volcán de Colima (Mexico). Unlike the granites analysed herein, the Darley Dale Sandstone sample (Figure 10a) contains pores (high aspect ratio features) and was deformed triaxially in the brittle regime until failure (under a confining pressure of 50 MPa and a pore fluid pressure (distilled water) of 20 MPa) in an experiment from Heap et al. (2009b). In this regime, failed samples of Darley Dale Sandstone typically show a shear band (that hosts intensely comminuted grains) and microcracks preferentially aligned to the direction of maximum principal stress outside the band (Wu et al., 2000). We find that the image processing performs well outside the shear band, isolating inter- and intra-granular microcracks (Figure 10b). We notice that the extent of microcracking increases with proximity to the shear band (Figure 10b). Inside of this shear band, however, no microcracks are located because the shear band constitutes a zone of crushed grains, rather than discrete fractures (the quantification of crack density within areas of grain crushing, automatically or otherwise, is beyond the scope of this study).

The andesite from Volcán de Colima was selected for analysis because it contains a network of naturally occurring microcracks within a groundmass that hosts crystals and irregularly-shaped pores (Farquharson et al., 2015; Heap et al., 2014a) (Figure 11a). Our algorithm works well at locating microcracks and crystal boundaries are correctly ignored (Figure 11b). However, the algorithm is unable to distinguish between pore boundaries and microcracks, which appear similar in this case. The algorithm will therefore overestimate the microcrack density and would need further development to avoid counting pore boundaries as microcracks. An alternative solution would be to use SEM micrographs of the andesite, where pore boundaries will appear much sharper.

Overall, we find that the procedure works well for microcracked rocks and therefore is useful for a wide range of applications.

#### 4.2 Evolution of microcrack characteristics and physical properties with thermal stressing temperature

Our microstructural characterisation of the thermally microcracked granites shows that the mean microcrack length increases slightly between the unheated and the 550 °C sample (from 56 to 72 µm), but the number of microcracks per unit area remains roughly constant (within the range of 64.4–

79.6/mm<sup>2</sup>), as the thermal stressing temperature is increased to 550 °C (Figure 3). Between 550 °C and 600 °C, the microcrack number density sharply increases to 140.4/mm<sup>2</sup> and the mean length sharply decreases to 61 µm (Figure 3). The 2D microcrack density,  $\gamma$ , is proportional to both the microcrack number density and the square of the microcrack length (Equation 3). We found that the measured microcrack density increases with temperature up to 600 °C (from 0.062 for the unheated sample to 0.131 for the 600 °C sample) and is roughly constant above 600 °C (between 0.13 and 0.14) (Figure 5b).

For temperatures of up to 600 °C, the aforementioned increase in microcrack density manifests as changes to the rock physical properties. In agreement with previous studies of the physical properties of thermally microcracked granite, our measurements (Figure 6) show that porosity increases (Chaki et al., 2008; David et al., 1999; Géraud, 1994; Nasser et al., 2009; Reuschlé et al., 2006) whilst  $v_p$  decreases (Chaki et al., 2008; David et al., 1999; Nasser et al., 2007; Reuschlé et al., 2006), and that the UCS decreases (Homand-Etienne and Houper, 1989), as a function of thermal stressing temperature. Further, we observe a large increase in porosity and a large decrease in  $v_p$  and UCS between the samples heated to 550 and 600 °C (Figure 6). This latter observation is due to the alpha-beta transition of quartz at around 573 °C, which is accompanied by a large expansion in volume and therefore increased inter-granular thermal stresses (Fredrich and Wong, 1986; Glover et al., 1995; Jones et al., 1997; Nasser et al., 2007). Although we see a decrease in UCS with thermal stressing temperature, it is worth noting that the influence of thermal microcracks on compressive strength decreases significantly under confinement (Violay et al., 2017; Wang et al., 2013).

Above 600 °C, the physical properties (porosity,  $v_p$ , and UCS) continue to evolve (Figure 6) whilst the measured microcrack density is almost constant (Figure 5b). One explanation for the constant microcrack density between thermal stressing temperatures of 600 and 900 °C is that cracks grow to a maximum length, depending on the lengthscale of the microstructure (i.e. the grain size). This does not seem to be the case, however, as the mean microcrack length (~60 µm) is much lower than the average grain size (~1 mm, Figure 1a). The low value for the mean microcrack length, compared to the average grain size, is likely due to the presence of intracrystalline microcracks, which are usually much smaller than the crystals (Kranz, 1983). Another possible explanation for the constant measured microcrack density could be that, at these high temperatures, microcracks are growing into one other, creating a mesh of microcracks that are considered as many individual microcracks by the algorithm. This would result in a decrease in microcrack length, but it would also result in an increase in microcrack number density, which we do not observe (Figure 3).



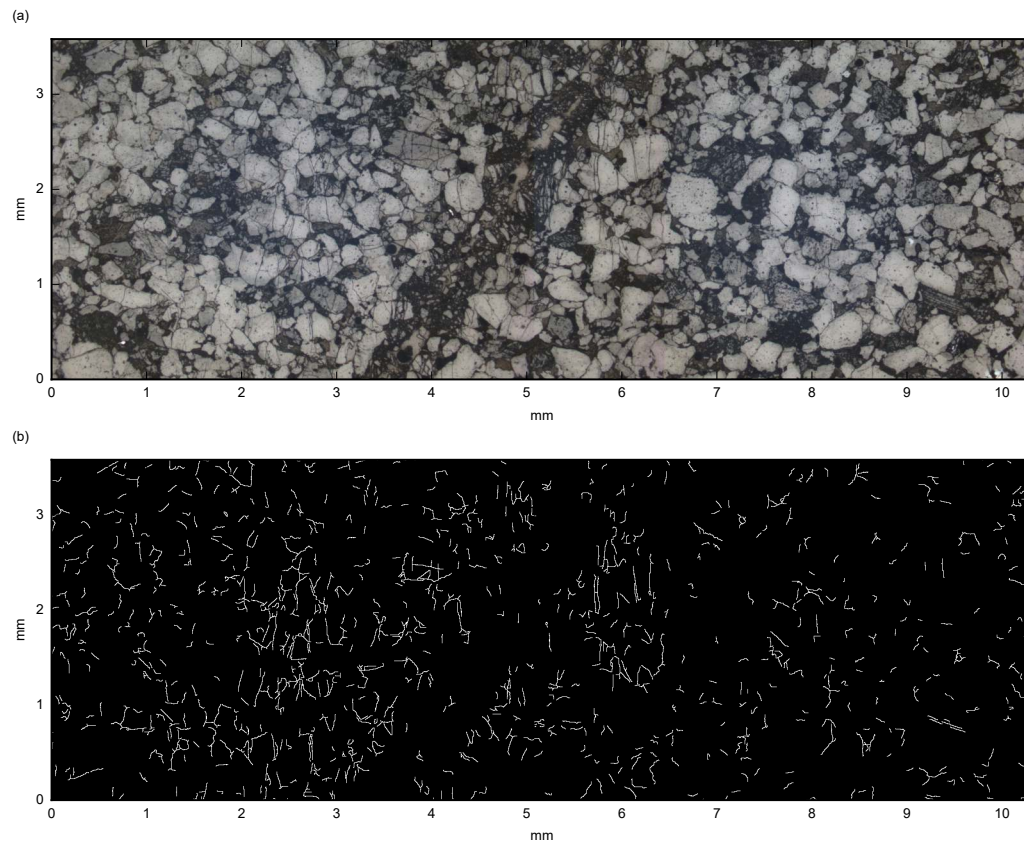


Figure 10: (a) Micrograph of Darley Dale Sandstone exhibiting strain localisation. The sandstone was deformed under a confining pressure of MPa and a pore pressure of 20 MPa pore pressure until failure (Heap et al., 2009b). (b) The results of the image analysis procedure. Cracks have been dilated to improve visibility for the reader.

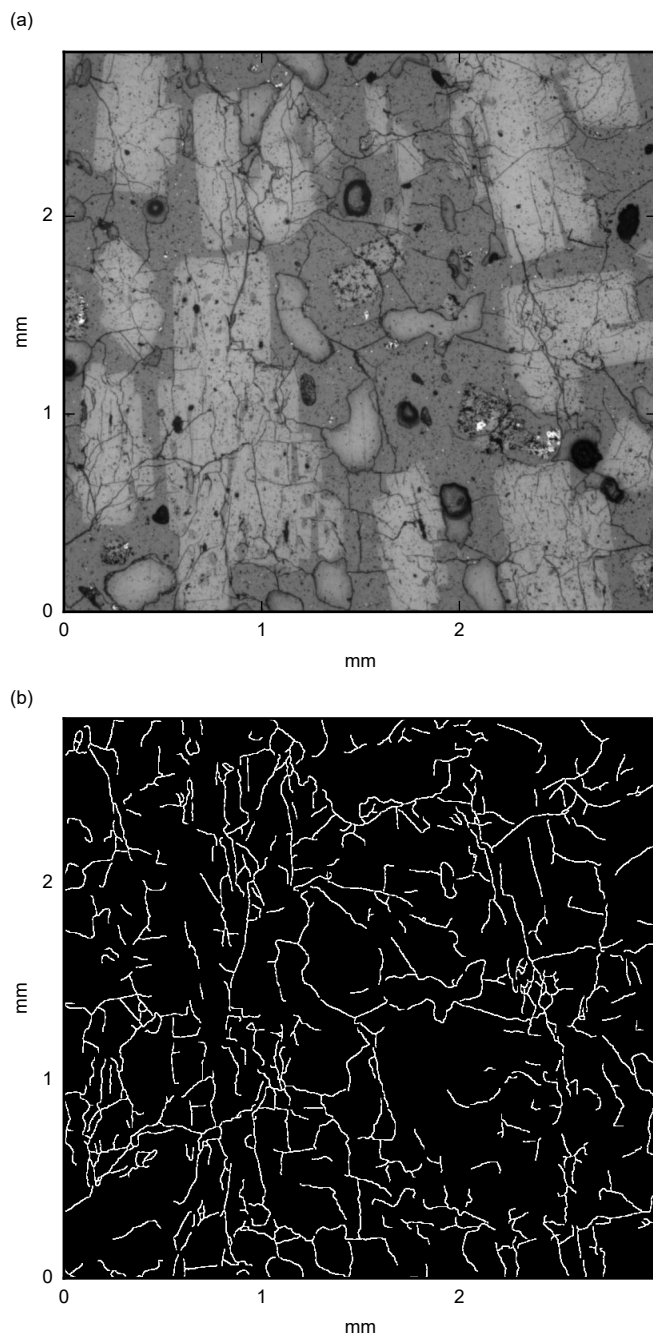


Figure 11: (a) Micrograph of thin section of andesite from Volcán de Colima (Mexico). (b) The results of the image analysis procedure. Cracks have been dilated to improve visibility for the reader.

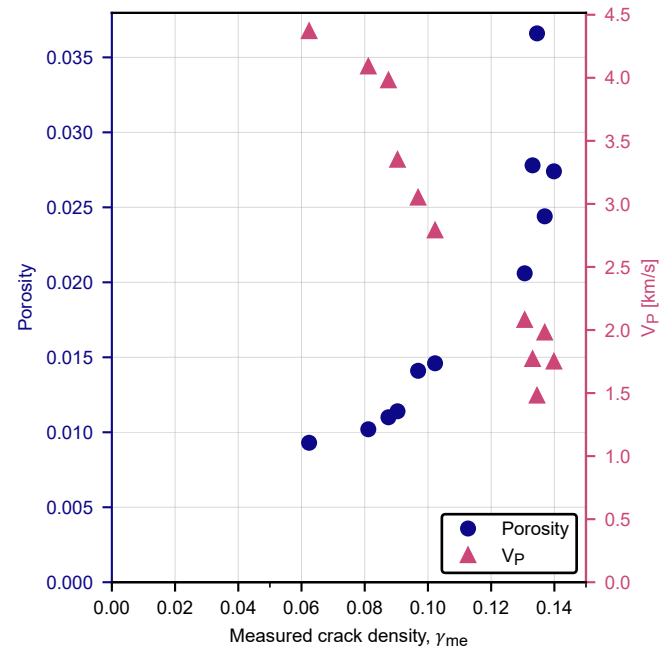


Figure 12: The measured porosity and P-wave velocity ( $v_p$ ) of the 11 Garibaldi Grey Granite samples against the measured crack density.

Another explanation for the low variation in the measured microcrack density values at high temperature could be that there is much less microcracking between temperatures of 600 and 900 °C. Although this explanation appears unlikely, because we observe changes to both the porosity and  $v_p$  between 600 and 900 °C (Figure 6a), perhaps there is an increase in the aperture of microcracks between these temperatures, rather than an increase in the number of microcracks. We can explore this further by plotting  $v_p$  and porosity as a function of the measured microcrack density (noted  $\gamma_{me}$  in Figure 12). We find that as microcrack density increases, we see a decrease in  $v_p$  and an increase in porosity. More specifically, the increase in porosity accelerates at higher microcrack densities. This observation could be explained by an increase in the aspect ratio of microcracks, rather than the growth of new microcracks. Indeed, studies of thermal microcracking in Westerly Granite suggest that thermal microcrack aperture greatly increases as temperature is increased above the quartz alpha-beta transition (Johnson et al., 1978; Nasser et al., 2007). Qualitatively, we observe this increase in microcrack aperture in the micrographs of samples heated to temperatures of 600 °C and above. The increase in microcrack aperture would explain how physical properties (Figure 6) continue to evolve as temperature is increased beyond 600 °C whilst the microcrack density (a function of the number of microcracks and their lengths) shows much less variation (Figure 5b).

#### 4.3 Upscaling: predicting uniaxial compressive strength from microstructural measurements

We used the Ashby and Sammis (1990) micromechanical model to predict the UCS of the thermally microcracked granite from the microcrack characteristics determined by our image analysis. These predicted values are in good agreement with our measured values for temperatures of up to 550 °C. However, the model overestimates the strength for 600 °C and above (Figure 8).

Our quantitative microstructural analysis shows that the number of microcracks per unit area and the microcrack length do not change significantly from 600 to 900 °C (Figure 3). Thus, the calculated values of microcrack density (Figure 5b) and therefore  $D_0$  (Figure 13) also do not change significantly from 600 to 900 °C. Since  $D_0$  and  $c$  are the only model parameters we update for in Equation 7, if they show no variation then neither will the predicted UCS (as shown in Figure 8).

A possible explanation for the overestimation of UCS for temperatures of 600 to 900 °C is that the fracture toughness  $K_{IC}$ , which we kept constant at  $0.54 \text{ MPa m}^{1/2}$ , decreases with temperature. Indeed, Nasser et al. (2007) show the fracture toughness of thermally microcracked Westerly Granite to decrease with thermal stressing temperature from  $1.43 \text{ MPa m}^{1/2}$  at ambient temperature, to  $0.22 \text{ MPa m}^{1/2}$  at 850 °C. They observe a large decrease in  $K_{IC}$  for temperatures above that of the quartz alpha-beta transition, which in our case would lead to a decrease in the predicted UCS (Equation 5). Below 600 °C, the difference between the measured and predicted UCS due to smaller variations in  $K_{IC}$  is small and likely therefore hidden by the natural sample variability.

#### 4.4 Downscaling: predicting microcrack characteristics from stress cycling experiments

We used the David et al. (2012) sliding crack to infer the microcrack characteristics of the rock using mechanical data from stress cycling experiments (example stress-strain curves are shown in Figure 7a). We find that the microcrack densities inferred from the model follow a similar trend to the direct measurements (Figure 13), despite a difference in magnitude. If we plot the inferred microcrack density ( $\gamma_{\text{mo}}$ ) against the measured microcrack density ( $\gamma_{\text{me}}$ ) (Figure 13b) we see a linear trend whereby the David et al. (2012) model overestimates the actual microcrack density systematically by a constant factor of around 55 (Figure 13). An explanation for the difference in magnitude could be that the model does not account for microcrack interactions, which may become significant at high crack densities. Indeed, David et al. (2012) also infers unexpectedly high microcrack densities from the sliding crack

model and highlights the importance of selecting an adapted effective medium theory to account for microcrack interaction.

The inferred microcrack aspect ratio inferred from the sliding crack model increases with temperature, and continues to do so for temperatures above the alpha-beta transition in quartz (~573 °C). As discussed previously, this increase in aspect ratio could explain why we continue to measure large changes in the physical properties of the rock for thermal stressing temperatures higher than 600 °C (Figure 6) whilst the measured microcrack density (a function of the length and number of cracks) shows much less variation (Figure 5b).

## 5 CONCLUSION

To look specifically at the role of microcrack density on the stiffness and strength of rock whilst keeping other rock attributes constant (such as the mineralogy and grain size), we chose to study a fine-grained granite (Garibaldi Grey Granite) in which we induced varying degrees of thermal damage (up to a temperature of 900 °C). We then quantified the 2D microcrack density using a newly developed algorithm to process optical micrographs to provide measurements of the number of microcracks per unit area and their lengths.

We measured an increase in microcrack density with thermal stressing temperature for temperatures of up to 600 °C. Above 600 °C, the measured microcrack density within the granite is roughly constant. Measurements of the physical properties of the granite showed an increase in porosity and a decrease in  $v_p$  with heating temperature for temperatures of up to 900 °C. We therefore measure variations in physical properties where the microcrack density (a function of the number and length of microcracks) shows little variation. We suggest that the continued evolution of physical properties at temperatures of 600 °C and above is due to a widening of existing microcracks rather than their formation or propagation.

Using a combined experimental and modelling approach, we bridge the gap between our measurements of microcrack density at the microscale, and our measurements of mechanical properties at the sample scale. First, we applied an upscaling approach using our calculated microcrack densities as an input in Ashby and Sammis (1990) sliding wing crack model to predict the uniaxial compressive strength of the granite. The UCS predictions are comparable with our laboratory measurements for granite thermally stressed to temperatures of below 600 °C. For the granite heated to 600 °C and above, the compressive strength is overestimated by the model, perhaps due to a decrease in fracture toughness above the alpha-beta transition of quartz. Next, we took a downscaling approach by using the sliding crack model of David et al. (2012) to infer microcrack density and mean microcrack aspect ratio from

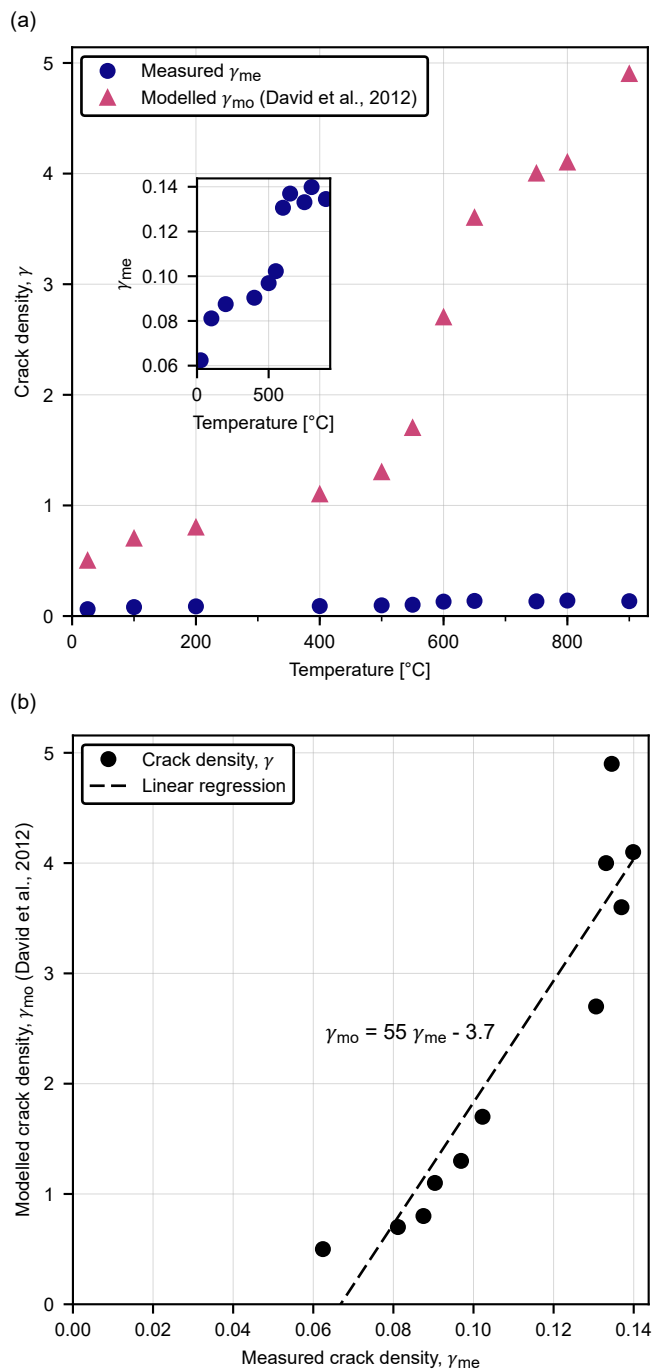


Figure 13: Comparison between crack densities from the David et al. (2012) sliding crack model and the optical measurements. (a) Inferred and measured microcrack densities as a function of thermal stressing temperature. Inset is a zoomed plot of the measured crack densities. (b) The inferred crack densities against the measured crack densities; the dashed line is their least squares linear regression.

laboratory measurements of stiffness. Whilst the inferred microcrack density ( $\gamma_{mo}$ ) is proportional to the measured microcrack density ( $\gamma_{me}$ ), the inferred values are greater by a factor of around 55 (Figure 13). A possible explanation for the difference is that the model does not account for microcrack interactions, which amplify their influence on rock stiffness.

Although we focused on the case of a fine-grained granite in this study, we propose the use of our image analysis procedure (see Supplementary Materials for details) for quantifying microcrack damage in rock types with vastly different microstructures. To demonstrate the power of the model, we analysed optical micrographs of a triaxially deformed sandstone (Darley Dale Sandstone) and a naturally microcracked andesite (from Volcán de Colima). Our method can accurately find the microcracks in both samples, although it falls short of characterising the grain crushing within the shear band of the sandstone sample, and treats some pore boundaries as microcracks in the andesite sample. Nevertheless, we anticipate that the image processing algorithm presented here will emerge as a useful tool in the quantification of microcrack characteristics in a range of microcracked materials and may be used provide input images for dedicated fracture pattern quantification tools such as FracPac (Healy et al., 2017).

Through the measurements and modelling presented in this study, we demonstrate how the microscale can inform on the laboratory or sample scale, and vice-versa. Uniting laboratory scale and microstructural observations through constrained up- and downscaling methods permits a deeper understanding of the mechanical behaviour of rocks.

## ACKNOWLEDGEMENTS

The authors would like to thank Bertrand Renaudié for sample preparation and Maximilien Charguéraud for his help with the laboratory measurements. This work has been published under the framework of LABEX grant ANR-11-LABX-0050\_G-EAU-THERMIE-PROFONDE and therefore benefits from state funding managed by the Agence Nationale de la Recherche (ANR) as part of the “Investissements d’avenir” program. We also acknowledge ANR grant CANTARE (ANR-15-CE06-0014-01). The authors would like to thank Thierry Reuschlé for his role in the development and maintenance of the laboratory equipment. We thank Kelly Russell and the members of VPL for their help in the acquisition of the testing material. The comments of two anonymous reviewers helped clarify several aspects of this manuscript.



## REFERENCES

- Arena, A., C. Delle Piane, and J. Sarout (2014). "A new computational approach to cracks quantification from 2D image analysis: Application to micro-cracks description in rocks". In: *Computers & Geosciences* 66, pp. 106–120. ISSN: 0098-3004. DOI: [10.1016/j.cageo.2014.01.007](https://doi.org/10.1016/j.cageo.2014.01.007).
- Ashby, M. F. and C. G. Sammis (1990). "The damage mechanics of brittle solids in compression". In: *Pure and Applied Geophysics* 133.3, pp. 489–521.
- Baud, P., T. Reuschlé, and P. Charlez (1996). "An improved wing crack model for the deformation and failure of rock in compression". In: *International journal of rock mechanics and mining sciences & geomechanics abstracts*. Vol. 33. Pergamon, pp. 539–542.
- Baud, P., T.-f. Wong, and W. Zhu (2014). "Effects of porosity and crack density on the compressive strength of rocks". In: *International Journal of Rock Mechanics and Mining Sciences* 67, pp. 202–211. ISSN: 1365-1609. DOI: [10.1016/j.ijrmms.2013.08.031](https://doi.org/10.1016/j.ijrmms.2013.08.031).
- Baud, P., A. Schubnel, and T.-f. Wong (2000). "Dilatancy, compaction, and failure mode in Solnhofen limestone". en. In: *Journal of Geophysical Research: Solid Earth* 105.B8, pp. 19289–19303. ISSN: 2156-2202. DOI: [10.1029/2000JB900133](https://doi.org/10.1029/2000JB900133).
- Bonnet, E., O. Bour, N. E. Odling, P. Davy, I. Main, P. Cowie, and B. Berkowitz (2001). "Scaling of fracture systems in geological media". en. In: *Reviews of Geophysics* 39.3, pp. 347–383. ISSN: 1944-9208. DOI: [10.1029/1999RG000074](https://doi.org/10.1029/1999RG000074).
- Brace, W. F., B. W. Paulding, and C. Scholz (1966). "Dilatancy in the fracture of crystalline rocks". en. In: *Journal of Geophysical Research* 71.16, pp. 3939–3953. ISSN: 2156-2202. DOI: [10.1029/JZ071i016p03939](https://doi.org/10.1029/JZ071i016p03939).
- Bérard, T. and F. Cornet (2003). "Evidence of thermally induced borehole elongation: a case study at Soultz, France". In: *International Journal of Rock Mechanics and Mining Sciences* 40.7-8, pp. 1121–1140. ISSN: 13651609. DOI: [10.1016/S1365-1609\(03\)00118-7](https://doi.org/10.1016/S1365-1609(03)00118-7).
- Bésuelle, P., J. Desrues, and S. Raynaud (2000). "Experimental characterisation of the localisation phenomenon inside a Vosges sandstone in a triaxial cell". In: *International Journal of Rock Mechanics and Mining Sciences* 37.8, pp. 1223–1237.
- Budiansky, B. and R. J. O'Connell (1976). "Elastic moduli of a cracked solid". In: *International Journal of Solids and Structures* 12.2, pp. 81–97. ISSN: 0020-7683. DOI: [10.1016/0020-7683\(76\)90044-5](https://doi.org/10.1016/0020-7683(76)90044-5).
- Chaki, S., M. Takarli, and W. Agbodjan (2008). "Influence of thermal damage on physical properties of a granite rock: Porosity, permeability and ultrasonic wave evolutions". In: *Construction and Building Materials* 22.7, pp. 1456–1461. ISSN: 0950-0618. DOI: [10.1016/j.conbuildmat.2007.04.002](https://doi.org/10.1016/j.conbuildmat.2007.04.002).
- Clauser, C. and E. Huenges (1995). "Thermal conductivity of rocks and minerals". In: *A Handbook of Physical Constants: Global Earth Physics* 3, pp. 105–126. ISSN: 0-87590-851-9. DOI: [10.1029/RF003p0105](https://doi.org/10.1029/RF003p0105).
- David, C., B. Menendez, and M. Darot (1999). "Influence of stress-induced and thermal cracking on physical properties and microstructure of La Peyratte granite". In: *International Journal of Rock Mechanics and Mining Sciences* 36.4, pp. 433–448.
- David, E. C., N. Brantut, A. Schubnel, and R. W. Zimmerman (2012). "Sliding crack model for nonlinearity and hysteresis in the uniaxial stress-strain curve of rock". In: *International Journal of Rock Mechanics and Mining Sciences* 52, pp. 9–17. DOI: [10.1016/j.ijrmms.2012.02.001](https://doi.org/10.1016/j.ijrmms.2012.02.001).
- Delle Piane, C., A. Arena, J. Sarout, L. Esteban, and E. Cazes (2015). "Micro-crack enhanced permeability in tight rocks: An experimental and microstructural study". In: *Tectonophysics*, pp. 1–8. DOI: [10.1016/j.tecto.2015.10.001](https://doi.org/10.1016/j.tecto.2015.10.001).
- Farquharson, J., M. J. Heap, N. R. Varley, P. Baud, and T. Reuschlé (2015). "Permeability and porosity relationships of edifice-forming andesites: A combined field and laboratory study". In: *Journal of Volcanology and Geothermal Research* 297, pp. 52–68. ISSN: 0377-0273. DOI: [10.1016/j.jvolgeores.2015.03.016](https://doi.org/10.1016/j.jvolgeores.2015.03.016).
- Fredrich, J. T. and T.-f. Wong (1986). "Micromechanics of thermally induced cracking in three crustal rocks". In: *Journal of Geophysical Research* 91.B12, pp. 12743–12743. ISSN: 0148-0227. DOI: [10.1029/JB091iB12p12743](https://doi.org/10.1029/JB091iB12p12743).
- Fredrich, J. T., B. Evans, and T.-f. Wong (1989). "Micromechanics of the brittle to plastic transition in Carrara marble". en. In: *Journal of Geophysical Research: Solid Earth* 94.B4, pp. 4129–4145. ISSN: 2156-2202. DOI: [10.1029/JB094iB04p04129](https://doi.org/10.1029/JB094iB04p04129).
- Germanovich, L. N., R. L. Salganik, A. V. Dyskin, and K. K. Lee (1994). "Mechanisms of brittle fracture of rock with pre-existing cracks in compression". In: *Pure and Applied Geophysics* 143.1, pp. 117–149.
- Glover, P. W. J., P. Baud, M. Darot, P. G. Meredith, S. A. Boon, M. LeRavalec, S. Zoussi, and T. Reuschlé (1995). "Alpha/Beta Phase Transitions in Quartz Monitored using Acoustic Emissions". In: *Geophysical Journal International* 120, pp. 775–782.
- Géraud, Y. (1994). "Variations of connected porosity and inferred permeability in a thermally cracked granite". en. In: *Geophysical Research Letters* 21.11, pp. 979–982. ISSN: 1944-8007. DOI: [10.1029/94GL00642](https://doi.org/10.1029/94GL00642).
- Griffith, A. A. (1921). "The phenomena of rupture and flow in solids". In: *Philosophical transactions of the royal society of london. Series A, containing papers of a mathematical or physical character* 221, pp. 163–198.
- Griffiths, L., M. J. Heap, T. Xu, C.-f. Chen, and P. Baud (2017). "The influence of pore geometry and orientation on the strength and stiffness of porous rock". In: *Journal of Struc-*

- tural Geology* 96, pp. 149–160. ISSN: 01918141. DOI: [10.1016/j.jsg.2017.02.006](#).
- Hadley, K. (1976). “Comparison of calculated and observed crack densities and seismic velocities in westerly granite”. en. In: *Journal of Geophysical Research* 81.20, pp. 3484–3494. ISSN: 2156-2202. DOI: [10.1029/JB081i020p03484](#).
- Hansen, A. and J. Schmittbuhl (2003). “Origin of the universal roughness exponent of brittle fracture surfaces: stress-weighted percolation in the damage zone”. In: *Physical review letters* 90.4, p. 045504.
- Hashin, Z. (1988). “The differential scheme and its application to cracked materials”. In: *Journal of the Mechanics and Physics of Solids* 36.6, pp. 719–734. ISSN: 0022-5096. DOI: [10.1016/0022-5096\(88\)90005-1](#).
- Healy, D., R. E. Rizzo, D. G. Cornwell, N. J. C. Farrell, H. Watkins, N. E. Timms, E. Gomez-Rivas, and M. Smith (2017). “FracPaQ: A MATLAB™ toolbox for the quantification of fracture patterns”. In: *Journal of Structural Geology* 95, pp. 1–16. ISSN: 0191-8141. DOI: [10.1016/j.jsg.2016.12.003](#).
- Heap, M. J., S. Vinciguerra, and P. G. Meredith (2009a). “The evolution of elastic moduli with increasing crack damage during cyclic stressing of a basalt from Mt. Etna volcano”. In: *Tectonophysics* 471.1-2, pp. 153–160. ISSN: 00401951. DOI: [10.1016/j.tecto.2008.10.004](#).
- Heap, M. J., P. Baud, P. G. Meredith, A. F. Bell, and I. G. Main (2009b). “Time-dependent brittle creep in Darley Dale sandstone”. In: *Journal of Geophysical Research: Solid Earth* 114.B7.
- Heap, M. J., Y. Lavallée, L. Petrakova, P. Baud, T. Reuschlé, N. R. Varley, and D. B. Dingwell (2014a). “Microstructural controls on the physical and mechanical properties of edifice-forming andesites at Volcán de Colima, Mexico”. en. In: *Journal of Geophysical Research: Solid Earth* 119.4, 2013JB010521. ISSN: 2169-9356. DOI: [10.1002/2013JB010521](#).
- Heap, M. J., T. Xu, and C.-f. Chen (2014b). “The influence of porosity and vesicle size on the brittle strength of volcanic rocks and magma”. In: *Bulletin of Volcanology* 76.9, pp. 1–15.
- Heap, M. J., F. B. Wadsworth, T. Xu, C.-f. Chen, and C. Tang (2016). “The strength of heterogeneous volcanic rocks: A 2D approximation”. en. In: *Journal of Volcanology and Geothermal Research* 319, pp. 1–11. ISSN: 03770273. DOI: [10.1016/j.jvolgeores.2016.03.013](#).
- Hill, R. (1952). “The elastic behaviour of a crystalline aggregate”. In: *Proceedings of the Physical Society. Section A* 65.5, p. 349.
- Homand-Etienne, F. and R. Houpert (1989). “Thermally induced microcracking in granites: characterization and analysis”. In: *International Journal of Rock Mechanics and Mining Sciences & Geomechanics Abstracts* 26.2, pp. 125–134. ISSN: 0148-9062. DOI: [10.1016/0148-9062\(89\)90001-6](#).
- Horii, H. and S. Nemat-Nasser (1986). “Brittle Failure in Compression: Splitting, Faulting and Brittle-Ductile Transition”. In: *Philosophical Transactions of the Royal Society A: Mathematical, Physical and Engineering Sciences* 319.1549, pp. 337–374. DOI: [10.1098/rsta.1986.0101](#).
- Jaeger, J. C., N. G. Cook, and R. Zimmerman (2009). *Fundamentals of rock mechanics*. John Wiley & Sons.
- Johnson, B., A. F. Gangi, J. Handin, and others (1978). “Thermal cracking of rock subjected to slow, uniform temperature changes”. In: *19th US Symposium on Rock Mechanics (USRMS)*. American Rock Mechanics Association.
- Jones, C., G. Keaney, P. Meredith, and S. Murrell (1997). “Acoustic emission and fluid permeability measurements on thermally cracked rocks”. In: *Physics and Chemistry of the Earth* 22.1, pp. 13–17. DOI: [10.1016/S0079-1946\(97\)00071-2](#).
- Kant, M. A., J. Ammann, E. Rossi, C. Madonna, D. Höser, and P. R. von Rohr (2017). “Thermal properties of Central Aare granite for temperatures up to 500°C: irreversible changes due to thermal crack formation”. en. In: *Geophysical Research Letters*, 2016GL070990. ISSN: 1944-8007. DOI: [10.1002/2016GL070990](#).
- Kemeny, J. M. and N. G. Cook (1991). “Micromechanics of deformation in rocks”. In: *Toughening mechanisms in quasi-brittle materials*. Springer, pp. 155–188.
- Kranz, R. L. (1983). “Microcracks in rocks: a review”. In: *Tectonophysics* 100.1-3, pp. 449–480.
- Le Ravalec, M., M. Darot, T. Reuschle, and Y. Gueguen (1996). “Transport properties and microstructural characteristics of a thermally cracked mylonite”. In: *pure and applied geophysics* 146.2, pp. 207–227.
- Mavko, G., T. Mukerji, and J. Dvorkin (2009). *The rock physics handbook: Tools for seismic analysis of porous media*. Cambridge university press.
- McClintock, F. A. and J. B. Walsh (1962). “Friction on Griffith cracks in rocks under pressure”. In: *Proc. 4th US Nat. Congr. Appl. Mech.* Vol. 2, pp. 1015–1022.
- Mitchell, T. M. and D. R. Faulkner (2009). “The nature and origin of off-fault damage surrounding strike-slip fault zones with a wide range of displacements: a field study from the Atacama fault system, northern Chile”. In: *Journal of Structural Geology* 31.8, pp. 802–816.
- Murrell, S. A. F. and P. J. Digby (1970). “The theory of brittle fracture initiation under triaxial stress conditions—II”. In: *Geophysical Journal International* 19.5, pp. 499–512.
- Nasseri, M. H. B., A. Schubnel, P. M. Benson, and R. P. Young (2009). “Common evolution of mechanical and transport properties in thermally cracked westerly granite at elevated hydrostatic pressure”. In: *Pure and Applied Geophysics* 166.5-7, pp. 927–948. ISSN: 0033-4553. DOI: [10.1007/s00024-009-0485-2](#).
- Nasseri, M., A. Schubnel, and R. Young (2007). “Coupled evolutions of fracture toughness and elastic wave velocities at high crack density in thermally treated Westerly granite”. In: *International Journal of Rock Mechanics and Mining Sciences* 44.4, pp. 601–616. ISSN: 1365-1609. DOI: [10.1016/j.ijrmms.2006.09.008](#).

- Ortiz, M. (1988). "Microcrack coalescence and macroscopic crack growth initiation in brittle solids". In: *International Journal of Solids and Structures* 24.3, pp. 231–250.
- Paterson, M. S. and T.-f. Wong (2005). *Experimental rock deformation-the brittle field*. Springer Science & Business Media.
- Rawling, G. C., P. Baud, and T.-f. Wong (2002). "Dilatancy, brittle strength, and anisotropy of foliated rocks: Experimental deformation and micromechanical modeling". en. In: *Journal of Geophysical Research: Solid Earth* 107.B10, p. 2234. ISSN: 2156-2202. DOI: [10.1029/2001JB000472](https://doi.org/10.1029/2001JB000472).
- Reuschlé, T., S. Gbaguidi Haore, and M. Darot (2006). "The effect of heating on the microstructural evolution of La Peyratte granite deduced from acoustic velocity measurements". In: *Earth and Planetary Science Letters* 243.3-4, pp. 692–700. DOI: [10.1016/j.epsl.2006.01.038](https://doi.org/10.1016/j.epsl.2006.01.038).
- Saltykov, S. A. (1958). "Stereometric metallography". In: *Metallurgizdat, Moscow* 267.
- Simmons, G. and D. Richter (1976). "Microcracks in rocks". In: *The physics and chemistry of minerals and rocks*, pp. 105–137.
- Simmons, G., T. Todd, and W. S. Baldrige (1975). "Toward a quantitative relationship between elastic properties and cracks in low porosity rocks". In: *American Journal of Science* 275.3, pp. 318–345.
- Siratovich, P. A., M. C. Villeneuve, J. W. Cole, B. M. Kennedy, and F. Bégué (2015). "Saturated heating and quenching of three crustal rocks and implications for thermal stimulation of permeability in geothermal reservoirs". In: *International Journal of Rock Mechanics and Mining Sciences* 80, pp. 265–280. ISSN: 1365-1609. DOI: [10.1016/j.ijrmms.2015.09.023](https://doi.org/10.1016/j.ijrmms.2015.09.023).
- Tapponnier, P. and W. F. Brace (1976). "Development of stress-induced microcracks in Westerly Granite". In: *International Journal of Rock Mechanics and Mining Sciences & Geomechanics Abstracts* 13.4, pp. 103–112. ISSN: 0148-9062. DOI: [10.1016/0148-9062\(76\)91937-9](https://doi.org/10.1016/0148-9062(76)91937-9).
- Underwood, E. E. (1967). "Quantitative Evaluation of Sectioned Material". en. In: *Stereology*. Ed. by H. Elias. DOI: [10.1007/978-3-642-88260-9\\_5](https://doi.org/10.1007/978-3-642-88260-9_5). Springer Berlin Heidelberg, pp. 49–60. ISBN: 978-3-540-03987-7 978-3-642-88260-9.
- Violay, M., M. J. Heap, M. Acosta, and C. Madonna (2017). "Porosity evolution at the brittle-ductile transition in the continental crust: Implications for deep hydro-geothermal circulation". In: *Scientific Reports* 7. ISSN: 2045-2322. DOI: [10.1038/s41598-017-08108-5](https://doi.org/10.1038/s41598-017-08108-5).
- Vosteen, H. and R. Schellschmidt (2003). "Influence of temperature on thermal conductivity, thermal capacity and thermal diffusivity for different types of rock". In: *Physics and Chemistry of the Earth* 28, pp. 499–509. DOI: [10.1016/S1474-7065\(03\)00069-X](https://doi.org/10.1016/S1474-7065(03)00069-X).
- Walsh, J. B. (1965). "The effect of cracks on the compressibility of rock". In: *Journal of Geophysical Research* 70.2, pp. 381–381. ISSN: 0148-0227. DOI: [10.1029/JZ070i002p00381](https://doi.org/10.1029/JZ070i002p00381).
- Wang, X.-Q., A. Schubnel, J. Fortin, Y. Guéguen, and H.-K. Ge (2013). "Physical properties and brittle strength of thermally cracked granite under confinement". In: *Journal of Geophysical Research: Solid Earth* 118, pp. 6099–6112. ISSN: 2169-9356. DOI: [10.1002/2013JB010340](https://doi.org/10.1002/2013JB010340).
- Wong, R. H. C., K. T. Chau, C. A. Tang, and P. Lin (2001). "Analysis of crack coalescence in rock-like materials containing three flaws—part I: experimental approach". In: *International Journal of Rock Mechanics and Mining Sciences* 38.7, pp. 909–924.
- Wong, T.-f. (1985). "Geometric probability approach to the characterization and analysis of microcracking in rocks". In: *Mechanics of Materials* 4.3, pp. 261–276. ISSN: 0167-6636. DOI: [10.1016/0167-6636\(85\)90023-7](https://doi.org/10.1016/0167-6636(85)90023-7).
- Wu, X. Y., P. Baud, and T.-f. Wong (2000). "Micromechanics of compressive failure and spatial evolution of anisotropic damage in Darley Dale sandstone". In: *International Journal of Rock Mechanics and Mining Sciences* 37.1–2, pp. 143–160. ISSN: 1365-1609. DOI: [10.1016/S1365-1609\(99\)00093-3](https://doi.org/10.1016/S1365-1609(99)00093-3).
- Zimmerman, R. W. (1985). "The effect of microcracks on the elastic moduli of brittle materials". In: *Journal of Materials Science Letters* 4.12, pp. 1457–1460. DOI: [10.1007/BF00721363](https://doi.org/10.1007/BF00721363).